

Indicator Cokriging-Based Subpixel Mapping Without Prior Spatial Structure Information

Qunming Wang, Peter M. Atkinson, and Wenzhong Shi

Abstract—Indicator cokriging (ICK) has been shown to be an effective subpixel mapping (SPM) algorithm. It is noniterative and involves few parameters. The original ICK-based SPM method, however, requires the semivariogram of land cover classes from prior information, usually in the form of fine spatial resolution training images. In reality, training images are not always available, or laborious work is needed to acquire them. This paper aims to seek spatial structure information for ICK when such prior land cover information is not obtainable. Specifically, the fine spatial resolution semivariogram of each class is estimated by the deconvolution process, taking the coarse spatial resolution semivariogram extracted from the class proportion image as input. The obtained fine spatial resolution semivariogram is then used to estimate class occurrence probability at each subpixel with the ICK method. Experiments demonstrated the feasibility of the proposed ICK with the deconvolution approach. It obtains comparable SPM accuracy to ICK that requires semivariogram estimated from fine spatial resolution training images. The proposed method extends ICK to cases where the prior spatial structure information is unavailable.

Index Terms—Indicator cokriging (ICK), land cover mapping, semivariogram, subpixel mapping (SPM), super-resolution mapping.

I. INTRODUCTION

MIXED pixels are a common phenomenon in remote sensing images [1]. How best to extract land cover information from mixed pixels is a key issue in land cover mapping, and many soft classification techniques have been developed for this purpose. Commonly used approaches include linear spectral mixture analysis [2], fuzzy *c*-means classifiers [3], artificial neural networks [4], *k*-nearest neighbor classifiers [5], and support vector machines [6], [7]. Soft classification can provide the proportion of land cover classes within mixed pixels but cannot provide the spatial location of the classes. Atkinson first suggested that subpixel mapping (SPM) [8], which is also termed super-resolution mapping [9] in the field of remote sens-

Manuscript received October 10, 2013; revised January 9, 2014; accepted May 1, 2014. Date of publication May 21, 2014; date of current version August 4, 2014. This work was supported in part by the Ministry of Science and Technology of China under Grant 2012BAJ15B04 and Project 2012AA12A305 and in part by the National Natural Science Foundation of China under Grants 41201451 and 41331175. (Corresponding author: W. Shi.)

Q. Wang is with the Department of Land Surveying and Geo-Informatics, The Hong Kong Polytechnic University, Kowloon, Hong Kong (e-mail: wqm11111@126.com).

P. M. Atkinson is with Geography and Environment, University of Southampton, Southampton SO17 1BJ, U.K. (e-mail: P.M.Atkinson@soton.ac.uk).

W. Shi is with the Department of Land Surveying and Geo-Informatics, The Hong Kong Polytechnic University, Kowloon, Hong Kong and also with Wuhan University, Wuhan 430072, China (e-mail: lswzshi@polyu.edu.hk).

Color versions of one or more of the figures in this paper are available online at <http://ieeexplore.ieee.org>.

Digital Object Identifier 10.1109/TGRS.2014.2321834

ing, can be achieved through the postprocessing of a soft classification to predict the distribution of classes at the subpixel scale. Based on spatial dependence theory, the most likely SPM map is assumed to be the one with greatest spatial correlation.

Over the past decades, SPM has received increasing attention, and various SPM algorithms have been developed, including linear optimization techniques [10], Hopfield neural network [11]–[14], genetic algorithm [15], pixel swapping algorithm (PSA) [16]–[21], subpixel/pixel spatial attraction models (SPSAMs) [22], [23], Markov random field [24]–[28], particle swarm optimization [29], and contouring methods [30], [31]. These methods do not necessarily require prior models of spatial structure for land cover and are mainly designed based on spatial dependence. Alternatively, some other SPM algorithms, such as the backpropagation neural network [32], [33], two-point histogram [34], and indicator cokriging (ICK) [35]–[37], need prior knowledge in terms of fine spatial resolution training images to build relevant models for classes. The backpropagation neural-network-based SPM approach extracts the relationship between coarse proportions (input neurons) and fine class labels (output neurons) from the training image. The two-point histogram-based method, introduced by Atkinson [34], extracts the two-point histogram for a given distance and direction lag from the training image. The randomly initialized subpixel map is gradually optimized to match the target two-point histogram. The ICK method extracts the indicator semivariogram from the training image, to calculate conditional probabilities of class occurrence at each subpixel. These learning-based algorithms are theoretically able to decrease the inherent uncertainty in SPM to some extent. In Boucher and Kyriakidis's earlier work [35] as well as our previous work [37], [38], the geostatistics-based ICK model has been demonstrated to be competent for SPM, which is free of iteration and needs few parameters. Similar to other learning-based SPM algorithms, ICK-based SPM is demanding in terms of its requirement for prior spatial structure information as follows.

- 1) The spatial resolution of the prior structure information needs to be the same as the target fine spatial resolution for SPM.
- 2) The prior spatial structure information needs to be representative of the studied area for SPM.

Jin *et al.* [36] presented an interesting work to extract a fine spatial resolution indicator semivariogram from a small representative local area rather than the entire image for ICK-based SPM. The results demonstrated that ICK produces comparable accuracy with those using a globally derived spatial structure. This method is still based on the existence of

fine spatial resolution training images. Recently, attention has turned to ways to obtain training images, from which prior spatial structure information can be extracted for land cover mapping. The training images can be obtained by the following approaches [39], [40].

- 1) Fine spatial resolution classified maps from other areas of similar spatial structure to the study area. For example, Boucher and Kyriakidis [41] utilized a fine spatial resolution land cover map of a nearby city (Foshan) for ICK-based SPM of Guangzhou.
- 2) Fine spatial resolution images of the study area that are captured by previous airborne or satellite sensor observation. These images are then classified to generate training images.
- 3) Manually drawn artificial training images associated with computer technology and the user's expert knowledge on the characteristics of land cover. In [42], a training image was drawn by hand according to the linear characteristics of roads for road extraction.
- 4) Other sources, such as land use maps, aerial photographs, and Google Earth, can also be used to derive training images.

Uncertainties in the aforementioned approaches are unavoidable. For example, due to the differences between two cities, such as economic condition, environment, government planning, etc., the characteristics of the land cover in two neighboring cities may not be the same. The land cover of the same area in different periods may also have different spatial structures, considering human activities (e.g., building construction and vegetation harvesting, planting, and regrowth), and natural changes (e.g., changes in rainfall and vegetation phenology), and so on [37]. More importantly, the sources of training images are not always accessible, or laborious work is needed to acquire training images even if access to them is available. Therefore, it is worthwhile to explore if some effective alternative can be provided for ICK-based SPM when such prior spatial structure information is unavailable.

For traditional ICK-based SPM, fine spatial resolution training images are used to extract semivariograms for each land cover class, to characterize their spatial pattern at the target fine spatial resolution. In this paper, the fine spatial resolution semivariogram for ICK-based SPM was estimated using coarse spatial resolution land cover proportion images. This information is automatically available since the coarse spatial resolution image of proportions provides the input data for the SPM process. Although the proportion images are at a coarse spatial resolution, they provide information on the spatial characteristics of the land cover classes. For each class, the initially acquired coarse spatial resolution semivariogram was converted to the equivalent at the target spatial resolution by deconvolution.

Deconvolution is a technique for deriving a point support semivariogram from the experimental semivariogram of areal data [43], [44]. It is frequently used in mining, where all areas are considered to have the same size and shape of support [45], [46]. The technique has been extended to cases where only irregular geographical units are available. Kyriakidis [47]

theoretically discussed the deconvolution of semivariograms when areal data supports change from place to place. Goovaerts [44] provided an example study to explore its practical implementation, by mapping lung cancer mortality rates in Indiana and the Western U.S. using units of different shape and size. This is also one of the few studies that explicitly present the deconvolution process.

In some fields, such as soil survey, disease mapping, and population mapping, it is common to represent variables on a point support, as observations on quasi-point supports are much smaller than the support of interest. However, this is not the case for satellite remote sensing. Remote sensing images are normally composed of regularly sized pixels that cover a positive finite area, producing a given spatial resolution. In this paper, by deconvolution, we mean the derivation of the fine spatial resolution semivariogram (via the point semivariogram) from the coarse spatial resolution semivariogram (areal semivariogram). In the deconvolution process, the coarse spatial resolution proportions are viewed as the available areal data, and the framework is based on regular geographical units. Deconvolution is an intermediate step toward ICK-based SPM. After deconvolution, the estimated fine spatial resolution semivariogram of each class is used for ICK to predict the probability of class occurrence at the subpixel level. SPM is finally realized according to the ICK-derived probability and the proportions constraint from the input soft classification.

The remainder of this paper is organized as follows: Section II briefly introduces the background of ICK-based SPM. Section III presents the principles of deconvolution of the semivariogram and its implementation. The results are provided in Section IV and discussed in Section V. Section VI concludes this paper.

II. ICK-BASED SPM

Suppose Y is the observed coarse spatial resolution image with N pixels and X is the subpixel map at the fine spatial resolution with M pixels. Here, $M/N = S^2$, and S is the zoom factor. Let v_m ($m = 1, 2, \dots, M$) be a subpixel, K be the number of classes in the studied area, and $F_k(V_n)$ be the k th ($k = 1, 2, \dots, K$) class proportion in a coarse pixel V_n ($n = 1, 2, \dots, N$).

A. Coarse-to-Coarse and Fine-to-Coarse Semivariograms

Let $\gamma_k(h)$ be the fine spatial resolution semivariogram of the k th class that characterizes the spatial pattern of the k th class. The fine-to-coarse spatial resolution semivariogram between the k th class at the fine pixel v_m and the k th class proportion $a_k(V_n)$ at the coarse pixel V_n is

$$\gamma_k^{vV}(v_m, V_n) = \frac{1}{S^2} \sum_{m'=1}^{S^2} \gamma_k(h_{mm'}) \quad (1)$$

where $h_{mm'}$ is the distance (in fine pixels) between the centroid of v_m and the centroid of any fine pixel $v_{m'}$ within V_n .

The coarse-to-coarse spatial resolution semivariogram between any two coarse pixels V_n and $V_{n'}$ is computed as

$$\gamma_k^{VV}(V_n, V_{n'}) = \frac{1}{S^4} \sum_{m=1}^{S^2} \sum_{m'=1}^{S^2} \gamma_k(h_{mm'}) \quad (2)$$

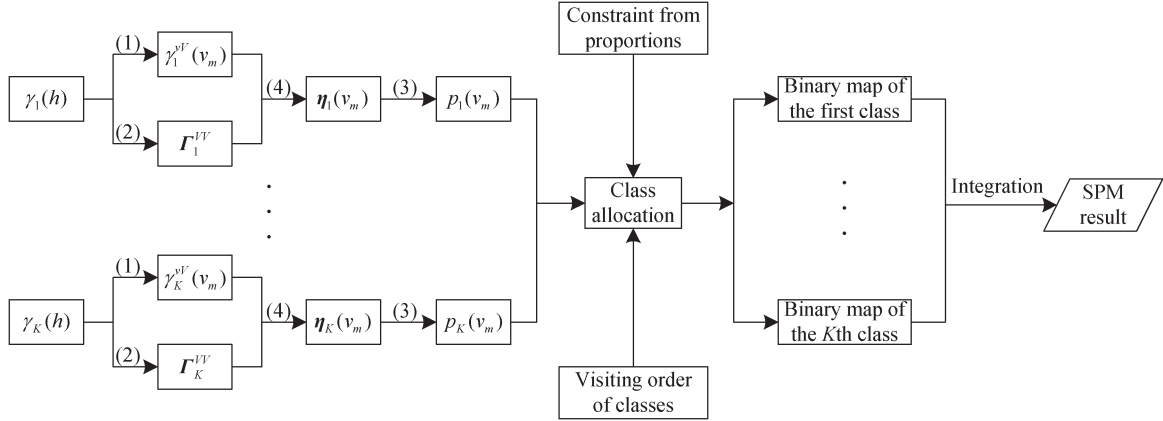


Fig. 1. Flowchart of the ICK-based SPM method in this paper.

where $h_{mm'}$ is the distance (in fine pixels) between the centroid of any fine pixel v_m within V_n and the centroid of any fine pixel $v_{m'}$ within $V_{n'}$.

B. ICK-Derived Probabilities

In this paper, we consider that the labels of all fine spatial resolution pixels are unknown (i.e., are not available from prior information) [36]. The ICK-derived probability $p_k(v_m)$, which means the probability of the k th class occurrence at subpixel v_m , is estimated as

$$P_k(v_m) = \boldsymbol{\eta}_k(v_m)^T \mathbf{F}_k + \pi_k [1 - \text{sum}(\boldsymbol{\eta}_k(v_m)^T)] \quad (3)$$

where $\mathbf{F}_k = [F_k(V_n), n = 1, 2, \dots, N]^T$ is an $(N \times 1)$ vector, π_k is the mean of all elements in vector \mathbf{F}_k , and the function $\text{sum}(\bullet)$ takes the sum of all the elements in vector \bullet . $\boldsymbol{\eta}_k(v_m)$ is an $(N \times 1)$ vector of contributions from N coarse pixels, which is computed by solving the following ICK equations [35]–[37]:

$$\boldsymbol{\Gamma}_k^{VV} \boldsymbol{\eta}_k(v_m) = \boldsymbol{\gamma}_k^{vV}(v_m) \quad (4)$$

where $\boldsymbol{\gamma}_k^{vV}(v_m)$ is an $(N \times 1)$ vector of fine-to-coarse spatial resolution semivariograms between subpixel v_m to be predicted and all N coarse pixels, i.e.,

$$\boldsymbol{\gamma}_k^{vV}(v_m) = [\gamma_k^{vV}(v_m, V_1), \gamma_k^{vV}(v_m, V_2), \dots, \gamma_k^{vV}(v_m, V_N)]^T \quad (5)$$

and $\boldsymbol{\Gamma}_k^{VV}$ is an $(N \times N)$ matrix of coarse-to-coarse spatial resolution semivariograms between all pairs of coarse pixel, i.e.,

$$\boldsymbol{\Gamma}_k^{VV} = \begin{bmatrix} \gamma_k^{VV}(V_1, V_1) & \gamma_k^{VV}(V_1, V_2) & \dots & \gamma_k^{VV}(V_1, V_N) \\ \gamma_k^{VV}(V_2, V_1) & \gamma_k^{VV}(V_2, V_2) & \dots & \gamma_k^{VV}(V_2, V_N) \\ \vdots & \vdots & \ddots & \vdots \\ \gamma_k^{VV}(V_N, V_1) & \gamma_k^{VV}(V_N, V_2) & \dots & \gamma_k^{VV}(V_N, V_N) \end{bmatrix}. \quad (6)$$

C. Allocating Class Labels to Subpixels

SPM is a hard classification technique (but at the subpixel scale), thereby generating thematic land cover maps. In SPM, the prior soft classification result acts as a constraint, and the

number of subpixels for the k th class with a coarse pixel V_n , which is denoted as $E_k(V_n)$, is determined as

$$E_k(V_n) = F_k(V_n)S^2. \quad (7)$$

Under the constraint in (7), the aforementioned ICK-derived probabilities (i.e., $p_k(v_m)$ ($k = 1, 2, \dots, K$; $m = 1, 2, \dots, M$)) are used to predict the class label of each subpixel. This process can be accomplished by a class allocation method developed in our recent work [38]. Based on the method, subpixels for each class are allocated in turn. For a particular class (e.g., the k th class), the $E_k(V_n)$ largest probabilities for it are selected, and the corresponding subpixels are allocated to the k th class. This way, K binary land cover maps will be generated, and they are finally integrated to produce the SPM result. The visiting order for all classes is determined by comparing Moran indexes of all K classes calculated from the class proportion images. The classes with higher indexes are visited before those with lower indexes. This class allocation method is fast and, more importantly, takes the intraclass spatial correlation into account. Fig. 1 is the flowchart of the presented ICK-based SPM method.

III. ESTIMATION OF FINE SPATIAL RESOLUTION SEMIVARIOGRAM WITHOUT PRIOR SPATIAL STRUCTURE INFORMATION

In Section II and Fig. 1, it can be found that the critical issue for ICK-based SPM is to obtain the fine spatial resolution semivariogram for each class. In the traditional ICK-based SPM model, the semivariogram sets $\gamma_1(h), \gamma_2(h), \dots, \gamma_K(h)$ are extracted from fine spatial resolution training images. Specifically, the training image of a studied area covering K classes can be decomposed into K binary land cover maps. The semivariogram $\gamma_k(h)$ can be acquired from the binary land cover map of the k th class. Here, the fine spatial resolution semivariogram sets are derived by deconvolution of the coarse spatial resolution semivariogram, and the whole process does not require any training images.

A. Objective of Deconvolution

Suppose $\gamma_k^V(h)$ is the coarse spatial resolution semivariogram calculated from the proportion image of the k th

class, i.e.,

$$\gamma_k^V(h) = \frac{1}{2N(h)} \sum_{n=1}^{N(h)} [F_k(V_n) - F_k(V_n + h)]^2 \quad (8)$$

where $N(h)$ is the number of paired pixels at a specific lag distance h (in coarse pixels) from the center pixel V_n . In this paper, the isotropic semivariogram is considered, and pixels at a specific distance from the center pixel in all directions are equally treated. With the scattered points, the continuous semivariogram function is fitted by the commonly used exponential model.

The fine spatial resolution semivariogram $\gamma_k(h)$ can be convolved to the coarse spatial resolution semivariogram $\gamma_k^{V-R}(h)$, which is also termed regularized semivariogram, by the well-known regularization [43]

$$\gamma_k^{V-R}(h) = \gamma_k^{VV}(V_n, V_n + h) - \gamma_k^{VV}(V_n, V_n) \quad (9)$$

where $\gamma_k^{VV}(V_n, V_n + h)$ is the coarse-to-coarse spatial resolution semivariogram, and $\gamma_k^{VV}(V_n, V_n)$, a constant for a given zoom factor S , is the average coarse spatial resolution semivariogram within a coarse pixel. Both of them are calculated using (2). Deconvolution aims to estimate the optimal fine spatial resolution semivariogram (denoted as $\gamma_k^{v-O}(h)$), the regularized semivariogram of which approximates $\gamma_k^V(h)$. The difference D between $\gamma_k^{V-R}(h)$ and $\gamma_k^V(h)$ is quantified by means of the root mean square error (RMSE). Thus

$$D = \sqrt{\frac{\sum_{l=1}^L [\gamma_k^{V-R}(h_l) - \gamma_k^V(h_l)]^2}{L}} \quad (10)$$

where L is the number of lag distances. Consequently, the objective of deconvolution is specifically to minimize the difference D in (10). Strictly, deconvolution is an ill-posed problem. Although one can obtain reassurance about regularizations (convolutions) of the fine spatial resolution semivariogram, one can never be sure that the estimated semivariogram is exactly the same as the true semivariogram of the studied area [39]. Deconvolution is employed in this paper to provide reliable inputs of class probability estimation for ICK-based SPM (see Fig. 1), rather than restoring an ideal fine spatial resolution semivariogram.

B. Implementation of Deconvolution

Deconvolution is an iterative process and contains two stages: initialization and update. Define I as an indicator as to whether the update of $\gamma_k^{v-O}(h)$ is successful: 1 means successful update, and 0 means unsuccessful update. In the whole process, the isotropic semivariogram is considered, and the commonly used exponential model is applied to fit the continuous semivariogram function. The detailed implementation is given as follows.

Stage 1: Initialization. The task of this stage is to initialize the optimal fine spatial resolution semivariogram $\gamma_k^{v-O}(h)$ and

obtain correspondingly the optimal regularized semivariogram $\gamma_k^{V-RO}(h)$ and optimal difference D^O .

- 1) Initialization of $\gamma_k^{v-O}(h)$. In this paper, the starting range of $\gamma_k^{v-O}(h)$ was the same as for $\gamma_k^V(h)$, the starting sill was double that for $\gamma_k^V(h)$, and the starting nugget was an empirical value $S/200$.
- 2) Regularization of $\gamma_k^{v-O}(h)$. The fine spatial resolution semivariogram $\gamma_k^{v-O}(h)$ is convolved to the regularized semivariogram $\gamma_k^{V-RO}(h)$ [see (9)].
- 3) Calculation of the difference between $\gamma_k^{V-RO}(h)$ and $\gamma_k^V(h)$. The optimal difference D^O in the initialization stage can be quantified by the RMSE between the two coarse spatial resolution semivariograms.
- 4) Initialization of indicator I . I is initialized to 1.

Stage 2: Update. This stage is implemented to update $\gamma_k^{v-O}(h)$ and modify it iteratively to minimize D^O .

- 1) Update of $\gamma_k^{v-O}(h)$. Each lag of the new fine spatial resolution semivariogram, denoted as $\gamma_k^{v-N}(h)$, is generated by

$$\gamma_k^{v-N}(h_l) = \gamma_k^{v-O}(h_l) + \rho_l [\gamma_k^V(h_l) - \gamma_k^{V-RO}(h_l)] \quad (11)$$

where ρ_l is an adaptive weight related to the iteration number, $\gamma_k^{v-O}(h)$ and indicator I .

If the update of $\gamma_k^{v-O}(h)$ in the last iteration is successful (i.e., $I = 1$), ρ_l is calculated as

$$\rho_l = \frac{\gamma_k^{v-O}(h_l)}{(C_1 + C_2)\sqrt{i}} \quad (12)$$

where C_1 and C_2 are the nugget and sill of $\gamma_k^{v-O}(h)$, and i is the number of current iteration. Take the first iteration as an example; ρ_l in (12) ranges from about 0 to 1 as l increases.

If the last update is unsuccessful (i.e., $I = 0$), ρ_l takes a smaller value for small adjustment of $\gamma_k^{v-O}(h)$ [44]

$$\rho_l = \frac{\gamma_k^{v-O}(h_l)}{2(C_1 + C_2)\sqrt{i}} \quad (13)$$

As the deconvolution iteratively proceeds, the weight ρ_l gradually decreases by dividing \sqrt{i} , and the adjustment of $\gamma_k^{v-O}(h)$ decreases. If the current optimal regularized semivariogram $\gamma_k^{V-RO}(h)$ is smaller than the target coarse spatial resolution semivariogram $\gamma_k^V(h)$, which indicates that the corresponding fine spatial resolution semivariogram $\gamma_k^{v-O}(h)$ is underestimated, an increase is produced in (11) for adjustment of $\gamma_k^{v-O}(h)$. In contrast, if $\gamma_k^{V-RO}(h)$ is greater than $\gamma_k^{v-O}(h)$, it indicates that $\gamma_k^{v-O}(h)$ is overestimated, and a decrease is produced in (11) for $\gamma_k^{v-O}(h)$. This flexible adjustment in (11) makes $\gamma_k^{V-RO}(h)$ approach the target $\gamma_k^V(h)$ gradually.

- 2) Regularization of $\gamma_k^{v-N}(h)$. The new fine spatial resolution semivariogram $\gamma_k^{v-N}(h)$ is convolved to the regularized semivariogram $\gamma_k^{V-RN}(h)$.

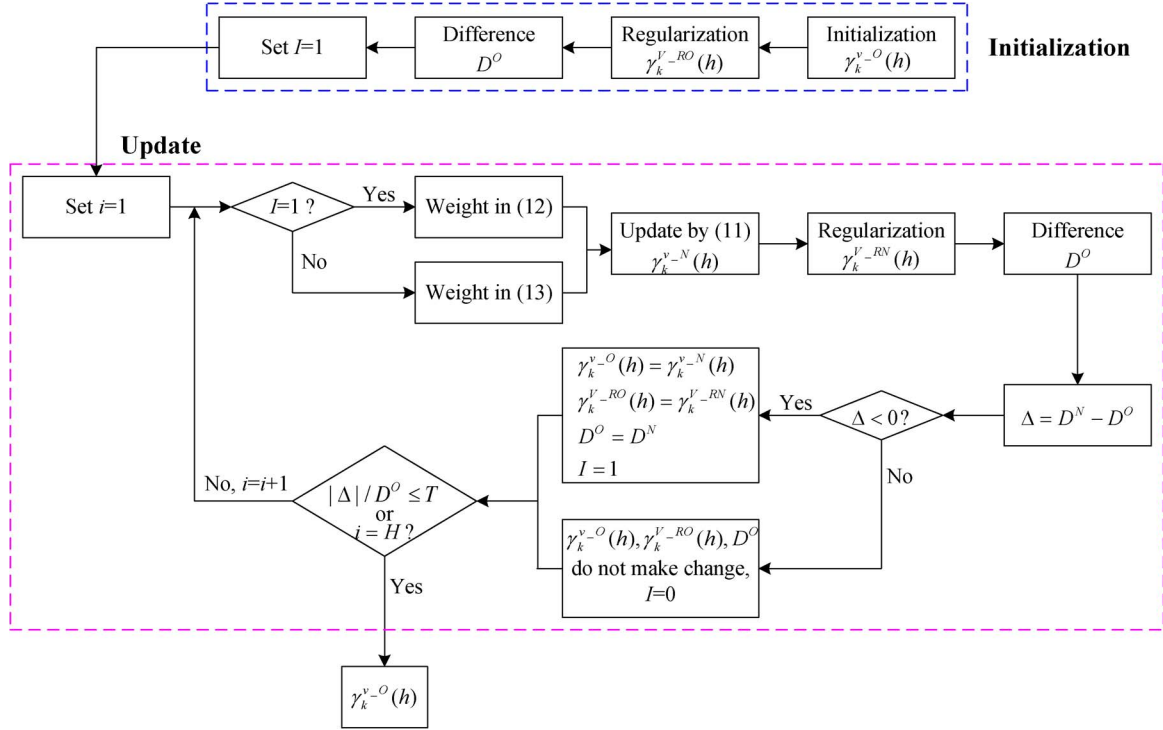


Fig. 2. Flowchart describing the process of semivariogram deconvolution.

- 3) Calculation of the difference between $\gamma_k^{v-RO}(h)$ and $\gamma_k^{v-O}(h)$. The new difference D^N is obtained by calculating the RMSE between the two semivariograms.
- 4) Determination of a new indicator I . D^O and D^N are compared by $\Delta = D^N - D^O$.

If $\Delta < 0$, it means that the update of $\gamma_k^{v-O}(h)$ is successful. Correspondingly, $\gamma_k^{v-O}(h)$ is updated by $\gamma_k^{v-RN}(h)$, $\gamma_k^{v-RO}(h)$ is updated by $\gamma_k^{v-RN}(h)$, and D^O is updated by D^N . Meanwhile, I is set to 1.

If $\Delta \geq 0$, it means that the update of $\gamma_k^{v-O}(h)$ is unsuccessful. In this case, $\gamma_k^{v-O}(h)$, $\gamma_k^{v-RO}(h)$, and D^O are not changed, and I is set to 0.

The new indicator I is used to guide the update of $\gamma_k^{v-O}(h)$ in the next iteration (i.e., whether (12) or (13) is applied). By step 4), the optimal semivariogram from the initialization to current iteration is retained, and the difference D is minimized as the deconvolution proceeds.

- 5) Termination of deconvolution. The deconvolution process is stopped when one of the following two conditions is met.
 - i) The number of iterations exceeds the maximum number H . In this paper, H was set to 20.
 - ii) The change in D^N in comparison with D^O is less than a small threshold T (e.g., 0.1% in this paper) for a consecutive three times, i.e.,

$$\frac{|\Delta|}{D^O} \leq T. \quad (14)$$

For all K classes, the aforementioned steps are carried out to produce the fine spatial resolution semivariogram sets $\gamma_1^{v-O}(h), \gamma_2^{v-O}(h), \dots, \gamma_K^{v-O}(h)$, which can then be used as inputs to ICK-based SPM, as presented in Fig. 1. Fig. 2 sum-

marizes the whole flowchart of deconvolution. As seen from the steps and in Fig. 2, the whole process of deconvolution needs no prior spatial structure information. The regularization process links the coarse spatial resolution semivariogram with the fine spatial resolution semivariogram, by involving the zoom factor S in (2). Therefore, the deconvolution approach is able to convert the coarse spatial resolution semivariogram to the desired target spatial resolution semivariogram.

IV. EXPERIMENTAL RESULTS

In the first two experiments, to avoid errors from soft classification and some other processes (e.g., registration) [48] and solely focus on the performance of SPM, the soft classification results were simulated by degrading the fine spatial resolution map with a mean filter. More precisely, the proportion image of each class was produced by degrading the binary map of that class in the fine spatial resolution map, with an $S \times S$ mean filter. This way, every $S \times S$ fine pixels were degraded to a coarse pixel. The third experiment was designed to gain a more realistic simulation of the coarse spatial resolution image and consider the uncertainty in soft classification. Specifically, a 30-m spatial resolution Landsat image was degraded band by band with a degradation factor to generate a coarse spatial resolution multispectral image. Soft classification (i.e., spectral unmixing) was then implemented to obtain proportion images, which were used as inputs to SPM (including the deconvolution process in the proposed method). The hard classification result of the 30-m Landsat image was considered as reference for SPM evaluation [9], [49].

The proposed ICK method that uses the semivariogram obtained by deconvolution was compared with the original

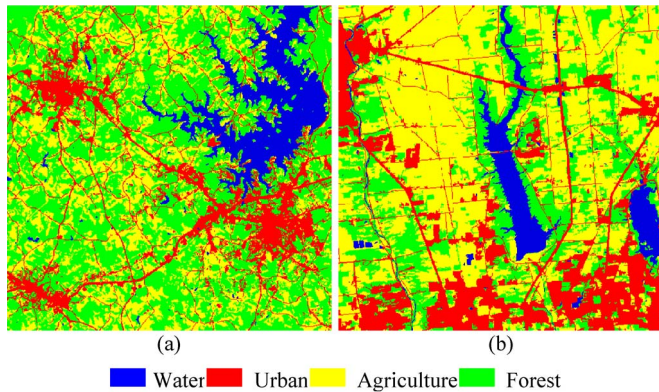


Fig. 3. Reference land cover maps in the first experiment. (a) South Carolina map. (b) Ohio map.

ICK method using fine spatial resolution training images. For clarity, we call the proposed method naive ICK (NICK). NICK was also compared with two well-known SPM algorithms (i.e., PSA [16]–[21] and SPSAM [22]) to validate its advantages in SPM. All experiments were tested on an Intel Core i7 Processor at 3.40 GHz with the MATLAB 7.1 version. PSA was implemented based on simulated annealing, and the number of iterations was set to 3000. For both ICK and NICK, a neighborhood window with 5×5 coarse pixels was considered for each coarse pixel for reasons of computational efficiency, as was done in [35] and [37].

A. Experiment 1

In the first experiment, two land cover maps from the National Land Cover Database 2001 (NLCD 2001) were tested. The NLCD 2001 is a raster-based land-cover classification with a medium spatial resolution of 30 m over all 50 U.S. states and Puerto Rico, which was produced using a set of data layers, including multiseason Landsat 5 and Landsat 7 images mostly acquired in 2001, digital elevation model-based derivatives, and other auxiliary data sets [36], [50]. Both land cover maps have a ground extent of $18 \text{ km} \times 18 \text{ km}$ and a size of 600×600 pixels. Four land cover classes are presented in the two maps: water, urban, agriculture, and forest. The first map covers an area in South Carolina, whereas the second map covers an area in Ohio, as shown in Fig. 3. It can be observed that the urban class in the two maps appears mainly as elongated features, whereas the water class appears mainly as large objects. In the South Carolina map, the pixels of the water, urban, agriculture, and forest classes occupy 9.74%, 16.27%, 26.76%, and 47.23%, respectively, of the entire image, and in the Ohio map, the corresponding proportions of the four classes are 6.33%, 23.32%, 45.88%, and 24.47%, respectively.

The two 30-m spatial resolution maps were degraded with five mean filters, i.e., 4×4 , 6×6 , 8×8 , 10×10 , and 12×12 , to simulate the 120-, 180-, 240-, 300-, and 360-m coarse spatial resolution proportion images of the four classes. The five different spatial resolution proportion images were used as the input for SPM, and the zoom factor S was correspondingly set to 4, 6, 8, 10, and 12, to restore the land cover map at 30-m spatial resolution.

We first take the 240-m spatial resolution image as an example for illustration and analysis. Fig. 4 gives the 240-m spatial

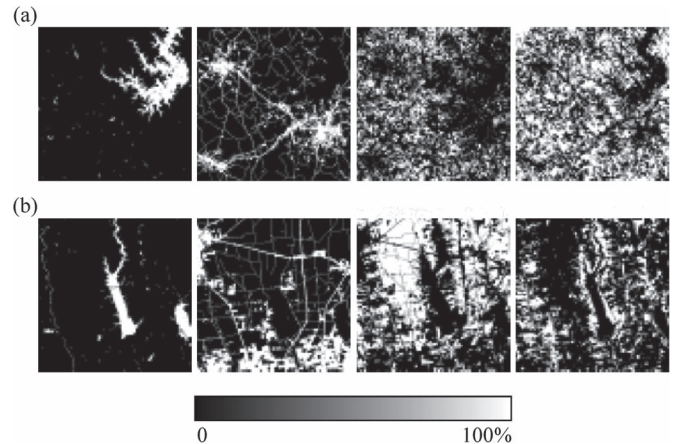


Fig. 4. Proportion images of the four classes in the simulated 240-m coarse spatial resolution images in experiment 1. From left to right: water, urban, agriculture, and forest. (a) South Carolina. (b) Ohio.

resolution proportion images created with a degradation factor of 8. It can be seen that the mixed pixels occur on the boundaries between classes, and the commonly existing blurry boundaries necessitate SPM techniques. The 30-m fine spatial resolution semivariograms of the two areas, which are estimated by deconvolving the coarse spatial resolution semivariograms extracted from the proportion images, are shown in Fig. 5. As can be observed from the semivariograms of each class in each coarse spatial resolution, the regularized coarse spatial resolution semivariogram (in green) and target coarse spatial resolution semivariogram (in blue) are highly similar and nearly coincide with each other in each case. This indicates the effectiveness of the deconvolution approach. It is worth noting that the nuggets of semivariograms at coarse spatial resolution (both regularized and target coarse semivariograms in Fig. 5) are smaller than that of the fine spatial resolution semivariogram. Moreover, for several classes, there are slight differences between the nuggets of the regularized semivariogram and the corresponding target coarse semivariogram. This is because deconvolution is an ill-posed problem, and the nugget of the fine spatial resolution semivariogram cannot be estimated from only the coarse spatial resolution semivariogram [46]. Additional information or expert knowledge on the characteristics of land cover may be a feasible source to solve this problem.

Using the estimated fine spatial resolution semivariogram, the class probabilities for each subpixel were then estimated by the ICK method. Fig. 6 exhibits the estimated ICK-derived probability maps of the four classes for the 240-m spatial resolution images in Fig. 4, based on the fine spatial resolution semivariograms in Fig. 5. Comparing the maps in Fig. 6 with Fig. 4, we can observe that the boundaries in Fig. 6 are much clearer than those presented in Fig. 4, suggesting that NICK is able to provide more detailed texture information than the proportion images.

The SPM results of the PSA, SPSAM, ICK, and NICK methods for the 240-m spatial resolution images of two studied areas are shown in Fig. 7. For ICK-based SPM of the two areas, the reference land cover maps in Fig. 3 were used as training images to extract the fine spatial resolution semivariogram. As

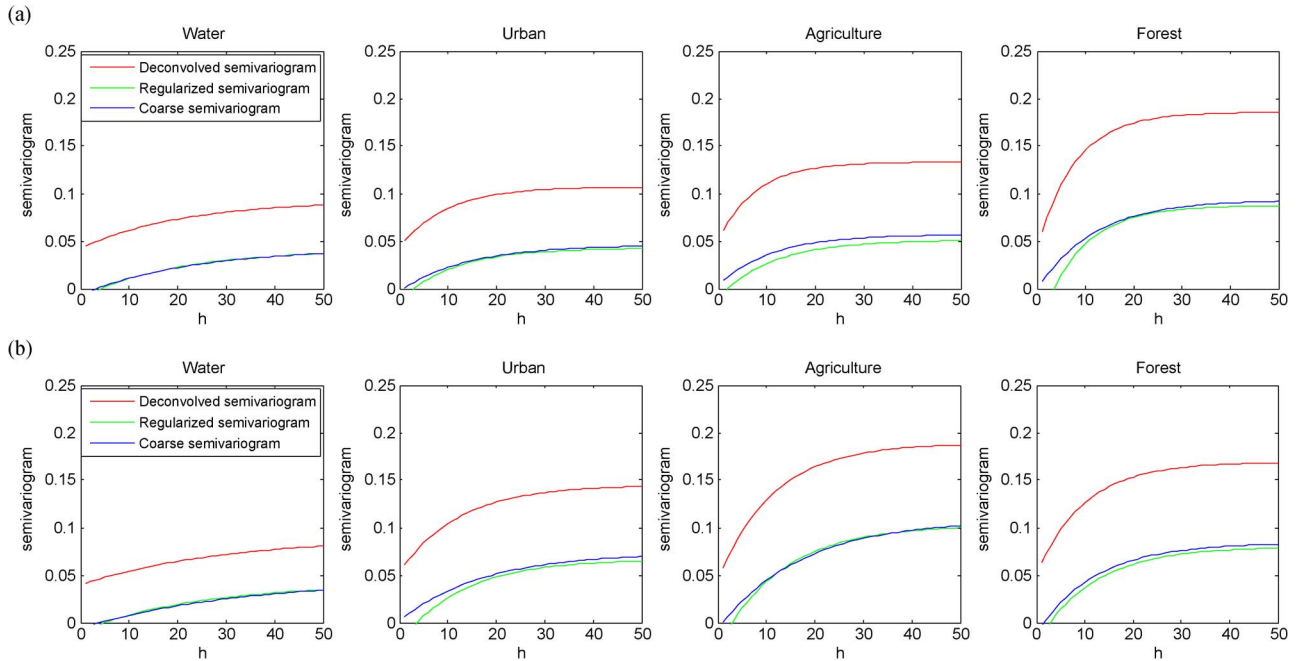


Fig. 5. Fine spatial resolution semivariogram obtained by deconvolution in experiment 1 ($S = 8$). The red, green, and blue curves denote the fine spatial resolution semivariogram from deconvolution, regularized coarse spatial resolution semivariogram, and coarse spatial resolution semivariogram extracted from the proportion image. (a) South Carolina. (b) Ohio.

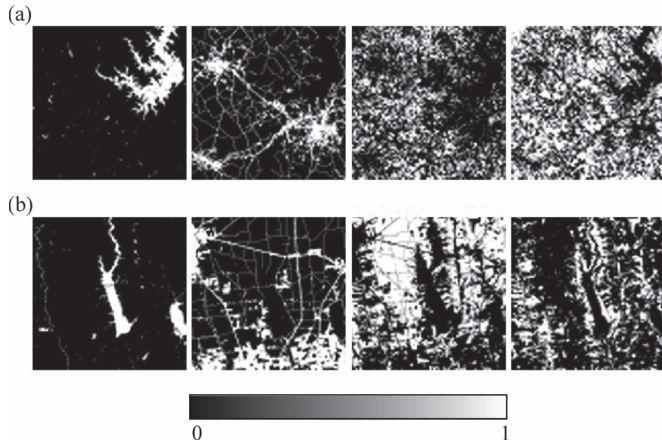


Fig. 6. ICK-derived probability maps of the four classes in experiment 1 ($S = 8$). From left to right: water, urban, agriculture, and forest. (a) South Carolina. (b) Ohio.

shown in Fig. 7(a) and (e), although the distribution of land cover in PSA results are smooth, there exist many disconnected and hole-shaped patches, particularly for the elongated urban class. Examining the SPSAM results, we can find many patches and linear artifacts in both resulting maps, and this phenomenon is particularly obvious for the urban class. The results of NICK are highly similar to those of ICK. Compared with PSA and SPSAM, both of them produce more continuous SPM results, which are more in agreement with the reference maps in Fig. 3. This can be illustrated well by the restoration of the urban class in the ICK and NICK results.

SPM is essentially a hard classification technique. Here, the performances of three methods for the 240-m spatial resolution images of two areas are also quantitatively evaluated by the classification accuracy of each class and the overall accuracy in

terms of the percentage of correctly classified pixels (PCC), as listed in Table I. Note that the nonmixed pixels were not considered in the accuracy statistics, since they will only increase the SPM accuracy without providing any useful information on the performance of the SPM methods [15], [37], [38], [51]–[53]. Checking the accuracy for each area in Table I, the accuracy of two geostatistics-based SPM approaches (i.e., ICK and NICK) is almost the same (PCC) as well as the accuracy for each class, and both of them are superior to PSA and SPSAM. In the South Carolina area, for NICK, the classification accuracy of the urban class is 62.02%, around 3% and 1% greater than that of PSA and SPSAM; the classification accuracy of the agriculture class is 63.34%, with gains of around 1.5% over PSA and SPSAM. With respect to the overall accuracy, PSA produces a PCC of 67.54%, whereas SPSAM produces a PCC of 67.77%. NICK increases the PCC by 1.2%. Focusing the results for the Ohio area, ICK and the proposed NICK again achieve similar accuracy for each class, which is higher than for PSA and SPSAM. The PCC of PSA and SPSAM increases from about 75.5% to 76.41% for the two geostatistics-based SPM methods.

In SPM, within each coarse pixel, the class labels of S^2 subpixels need to be predicted, and the performance of NICK is affected by the zoom factor S . Likewise, the four SPM methods are tested for the other four zoom factors, i.e., 4, 6, 10, and 12. The PCC of the four methods for all five zoom factors is shown in the bar chart in Fig. 8. It is worth noting that as S increases, the accuracy of all four methods decreases. Consistent with the results in Table I, in ten cases, NICK produces almost identical accuracy to ICK and higher PCC than PSA and SPSAM, which further validates the effectiveness of deconvolution of coarse spatial resolution semivariograms from the proportion images for ICK-based SPM.

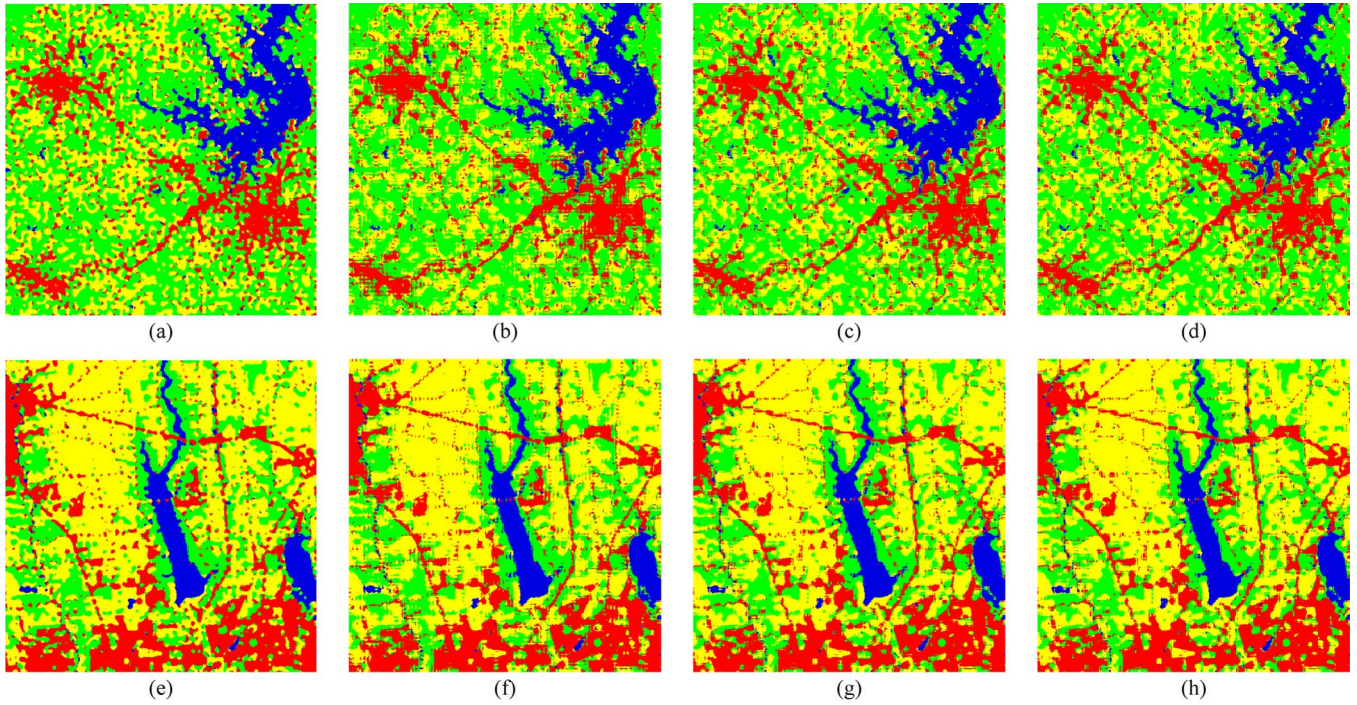


Fig. 7. SPM results in experiment 1 ($S = 8$). (a) and (e) PSA results. (b) and (f) SPSAM results. (c) and (g) ICK results. (d) and (h) NICK results. (a)–(d) South Carolina results. (e)–(h) Ohio results.

TABLE I
ACCURACY (%) OF SPM METHODS FOR THE SOUTH CAROLINA AND OHIO AREAS IN EXPERIMENT 1 ($S = 8$)

	South Carolina area				Ohio area			
	PSA	SPSAM	ICK	NICK	PSA	SPSAM	ICK	NICK
Water	80.16	80.34	81.06	81.07	75.58	76.60	77.22	77.20
Urban	59.15	61.05	62.02	62.02	72.68	72.84	73.30	73.31
Agriculture	61.69	61.90	63.30	63.34	79.32	79.52	80.33	80.33
Forest	72.54	72.19	73.40	73.42	72.14	71.77	72.93	72.94
PCC	67.54	67.77	68.97	68.99	75.52	75.58	76.41	76.41

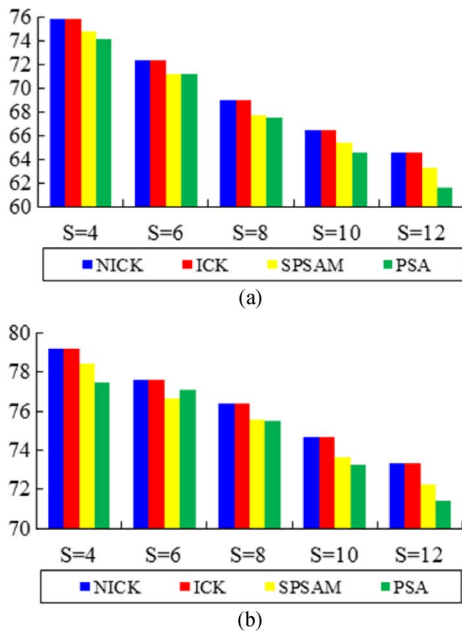


Fig. 8. PCC (%) of the four SPM methods in relation to zoom factor S in two areas. (a) South Carolina. (b) Ohio.



Fig. 9. Two QuickBird images used in experiment 2. (Left) Original images. (Right) Classified land cover maps. (a) Xuzhou suburban area. (b) Xuzhou urban center area.

B. Experiment 2

In the second experiment, two fine spatial resolution (0.61 m) QuickBird images were used to test the NICK approach. The two QuickBird images contain 480×480 pixels and three multispectral bands (RGB) and were acquired in

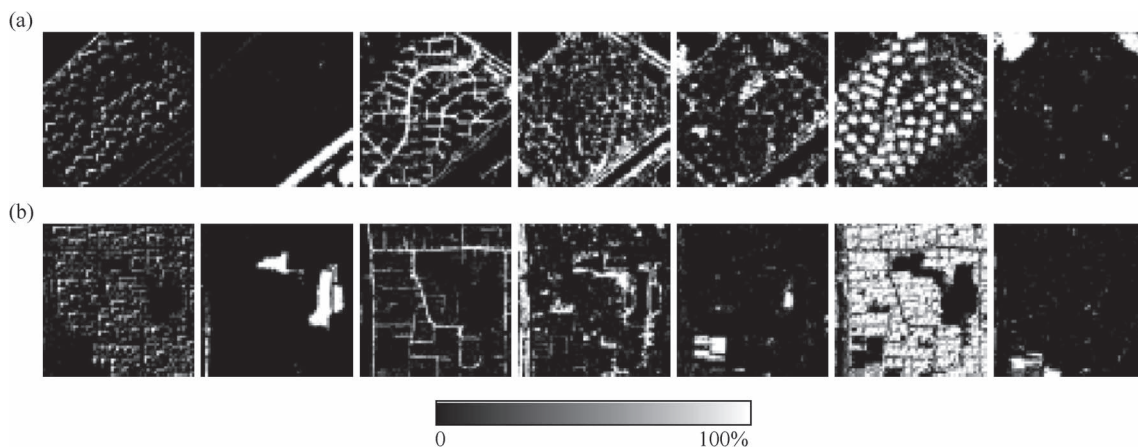


Fig. 10. Proportion images of the seven classes in the simulated 5-m coarse spatial resolution images. From left to right: shadow, water, road, tree, grass, roof, and bare soil. (a) Xuzhou suburban area. (b) Xuzhou urban center area.

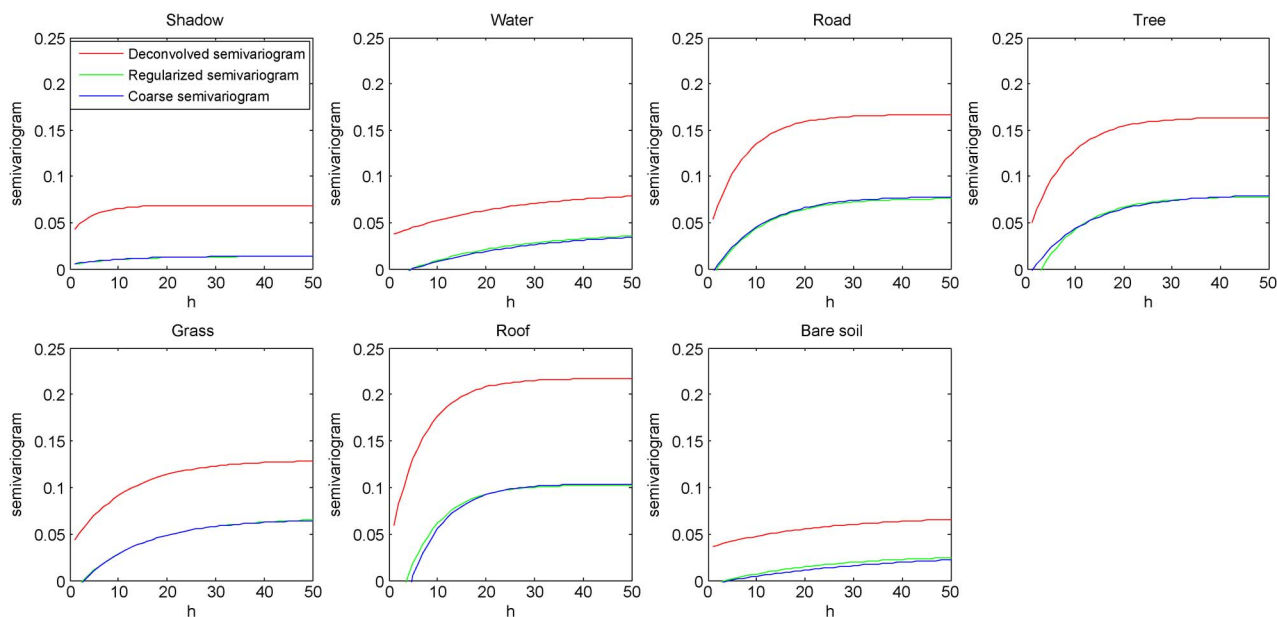


Fig. 11. Fine spatial resolution semivariogram obtained by deconvolution for the Xuzhou suburb area in experiment 2 ($S = 8$). The red, green, and blue curves denote the fine spatial resolution semivariogram from deconvolution, regularized coarse spatial resolution semivariogram, and coarse spatial resolution semivariogram extracted from the proportion image.

August 2005. One image covers the suburb of Xuzhou City, China, whereas the other image covers the urban center area of that city [54]. The two images were classified with an algorithm that first integrated spatial features of pixel shape feature set, gray-level cooccurrence matrix, and Gabor transform with spectral information and then used a support vector machine for classification. Each generated land cover map contains seven classes: shadow, water, road, tree, grass, roof, and bare soil. Fig. 9 shows the two original QuickBird images and the corresponding classified land cover maps.

The land cover maps in Fig. 9 were degraded with an 8×8 mean filter, producing two 5-m (relatively) coarse spatial resolution images, as shown in Fig. 10. The task of SPM in this experiment was to reproduce the two 0.61-m land cover maps from the simulated 5-m proportion images of seven classes. Fig. 11 shows the 0.61-m fine spatial resolution semivariograms

of the Xuzhou suburb area that were estimated by deconvolution. Likewise, the regularized coarse spatial resolution semivariogram and target coarse spatial resolution semivariogram are very similar to each other in each case. Fig. 12 gives the SPM results of the PSA, SPSAM, ICK, and NICK methods. The fine spatial resolution semivariograms for ICK were extracted from the reference maps in Fig. 9. As can be observed from both PSA results, the land cover is generally over-compact, leading to locally smooth and hole-shaped artifacts. With respect to two SPSAM results, some disconnected and cone-shaped patches exist, which conflicts with the spatial characteristics in Fig. 9. In the ICK and NICK results, this phenomenon is alleviated. As an example, in Fig. 12(c), (d), (g), and (h), the road class is more continuous, and the boundary of the roof class is smoother. Table II gives the classification accuracy of each class as well as the PCC for the four SPM

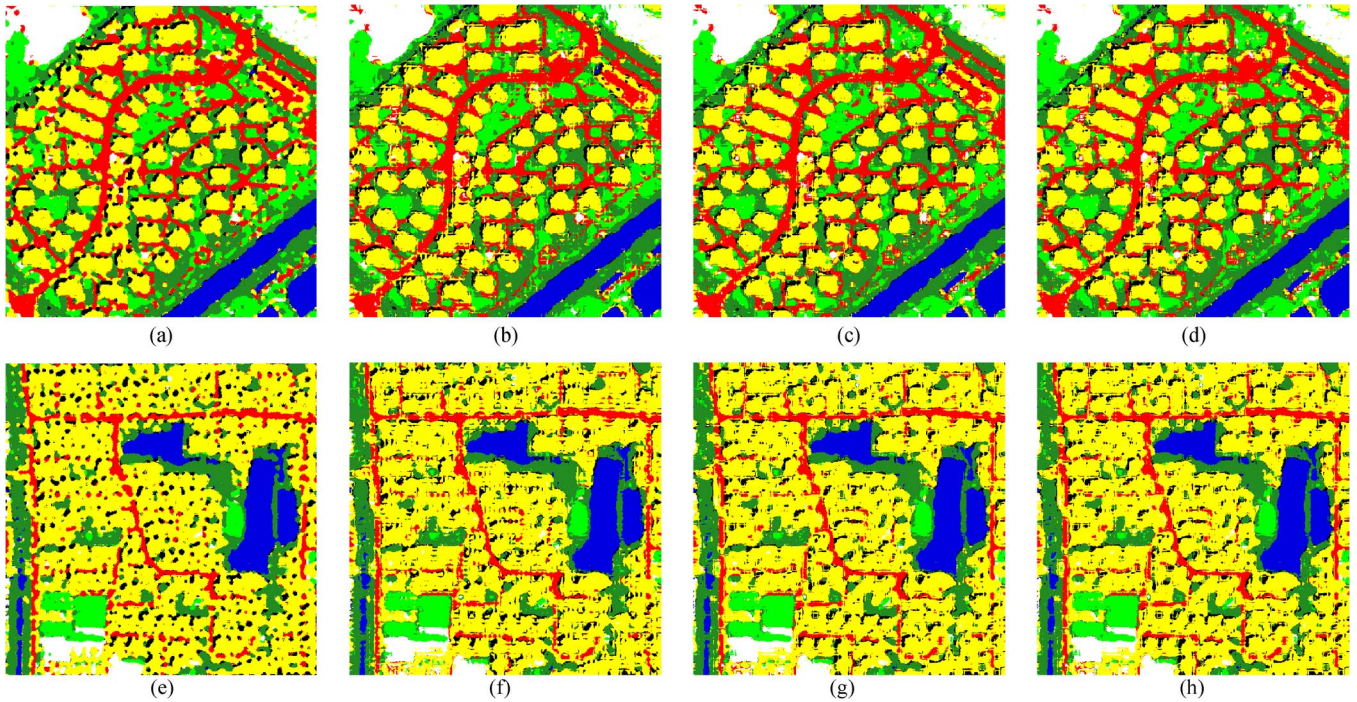


Fig. 12. SPM results in experiment 2 ($S = 8$). (a) and (e) PSA results. (b) and (f) SPSAM results. (c) and (g) ICK results. (d) and (h) NICK results. (a)–(d) Xuzhou suburban area results. (e)–(h) Xuzhou urban center area results.

TABLE II
ACCURACY (%) OF SPM METHODS FOR THE TWO XUZHOU AREAS IN EXPERIMENT 2 ($S = 8$)

	Xuzhou suburb area				Xuzhou urban center area			
	PSA	SPSAM	ICK	NICK	PSA	SPSAM	ICK	NICK
Shadow	54.91	50.92	53.26	53.13	36.03	36.30	38.27	37.99
Water	90.90	91.04	91.20	91.25	85.93	85.34	85.26	85.29
Road	77.34	74.24	75.73	75.74	64.41	61.98	62.20	62.23
Tree	73.77	71.93	73.41	73.41	77.70	77.20	77.75	77.80
Grass	70.63	70.76	71.70	71.71	67.18	69.26	68.75	68.75
Roof	73.63	72.79	73.84	73.81	80.71	80.64	81.01	80.98
Bare soil	75.92	78.17	77.52	77.54	59.89	61.71	62.05	62.05
PCC	73.37	71.88	73.12	73.10	74.09	73.84	74.30	74.28

methods. Again, the nonmixed pixels were not considered in the accuracy statistics. Regarding PSA, it produces higher accuracy for the shadow, road, and tree classes and greater PCC than the ICK and NICK methods in the Xuzhou suburban area. In the Xuzhou urban center area, although PSA has higher accuracy for the water and road classes, the PCC of PSA is lower than for the ICK and NICK methods. Checking the values for SPSAM, it has higher accuracy for the bare soil class in the Xuzhou suburban area and the grass class in the Xuzhou urban center area than ICK and NICK, but the classification of the other six classes is less accurate. The overall accuracy of ICK and NICK is greater than that of SPSAM. Moreover, ICK and NICK have comparable accuracy for all seven classes.

C. Experiment 3

A 30-m spatial resolution multispectral image acquired by the Landsat-7 enhanced thematic mapper plus (ETM+) sensor in August 2001 was used in this experiment. The image covers

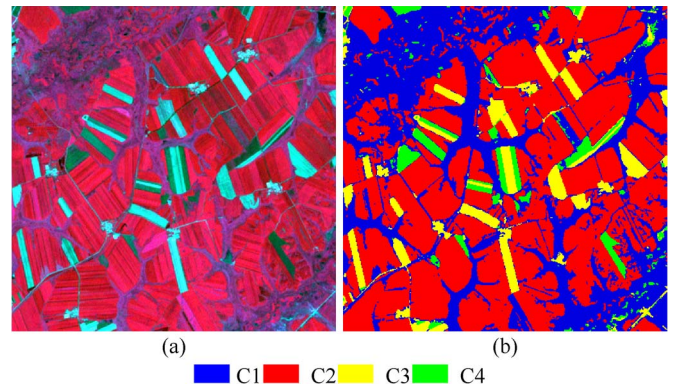


Fig. 13. Landsat images used in experiment 3. (a) Original images (bands 4, 3, and 2 as RGB). (b) Classified land cover maps.

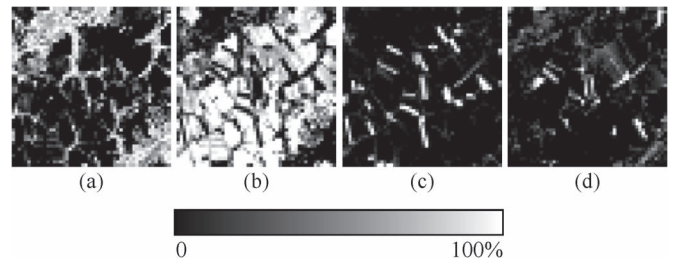


Fig. 14. Proportion images of the four classes obtained by spectral unmixing of the 240-m coarse images in experiment 3. (a) C1. (b) C2. (c) C3. (d) C4.

an area in the Liaoning Province, China and has a size of 400×400 pixels. Bands 1, 2, 3, 4, 5, and 7 of the Landsat image were used in the experiment. Four land cover classes were identified, and we denote them as C1, C2, C3, and C4. The false color image is shown in Fig. 13(a). The 30-m hard-classified land cover map in Fig. 13(b) was used as reference

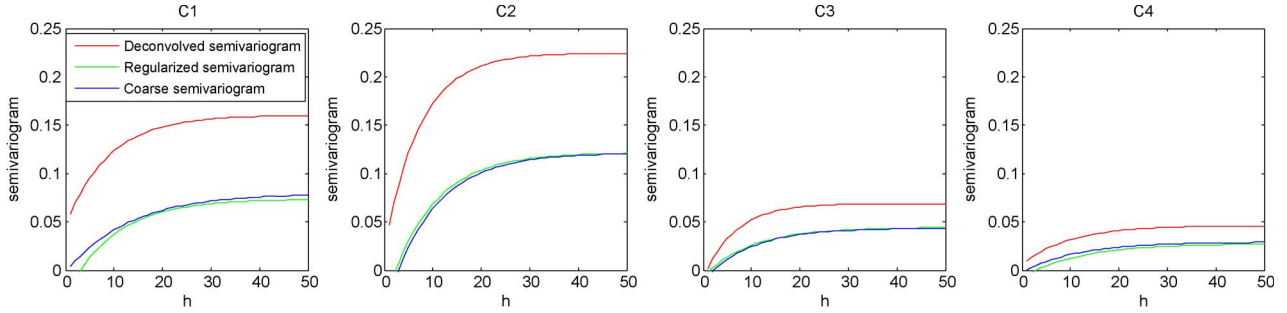


Fig. 15. Fine spatial resolution semivariogram obtained by deconvolution in experiment 3 ($S = 8$). The red, green, and blue curves denote the fine spatial resolution semivariogram from deconvolution, regularized coarse spatial resolution semivariogram, and coarse spatial resolution semivariogram extracted from the proportion image.

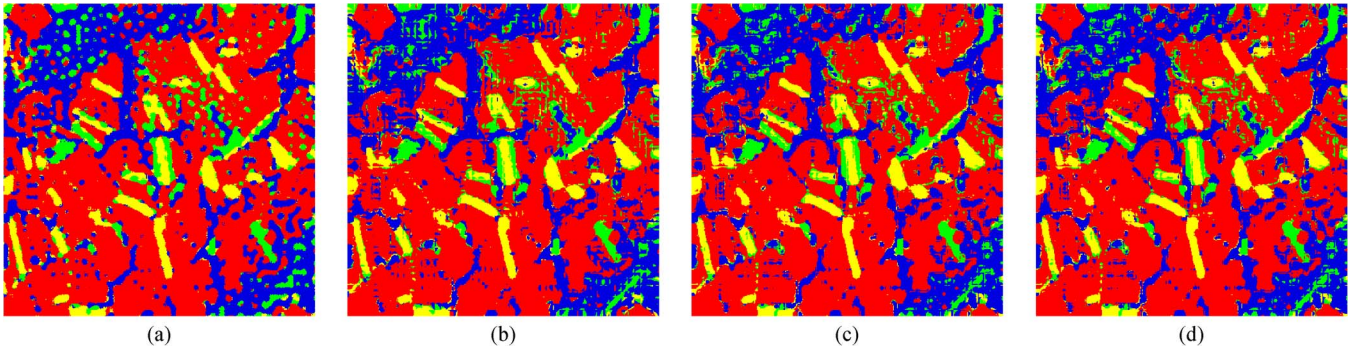


Fig. 16. SPM results in experiment 3 ($S = 8$). (a) PSA result. (b) SPSAM result. (c) ICK result. (d) NICK result.

for SPM evaluation, which was generated by a maximum-likelihood classification of the 30-m multispectral image (with an overall accuracy of over 90%).

The 30-m multispectral image was degraded via an 8×8 pixel mean filter to simulate an image with coarse (240 m) spatial resolution, comparable to the spatial resolution of medium-spatial-resolution systems such as Moderate Resolution Imaging Spectroradiometer (MODIS). Fully constrained least squares linear spectral mixture analysis [2], [55] has a simple physical meaning and has gained its popularity in application. In this experiment, it was employed for spectral unmixing. The predicted proportion images of the four classes are shown in Fig. 14. Fig. 14 is compared with the reference proportions (obtained by degrading Fig. 13(b) with an 8×8 mean filter) by means of the RMSE. The values for C1, C2, C3, and C4 are 0.1930, 0.1551, 0.0555, and 0.1091, which are relatively small errors.

Fig. 15 exhibits the deconvolved fine spatial resolution (30 m) semivariograms, along with the regularized coarse spatial resolution (240 m) semivariograms and target coarse semivariograms (240 m) extracted in Fig. 14. For each class, the 240-m regularized semivariogram and target coarse semivariogram are very similar to each other. For the four classes, the differences between the deconvolved semivariograms and reference fine spatial resolution semivariograms extracted in Fig. 13(b) are quantified by the RMSE, and the values are 0.0257, 0.0055, 0.0022, and 0.0046, suggesting that the deconvolved semivariograms are highly similar to the reference semivariograms. The high similarity is attributed mainly to the

TABLE III
ACCURACY (%) OF SPM METHODS IN EXPERIMENT 3 ($S = 8$)

	PSA	SPSAM	ICK	NICK
C1	61.85	61.71	62.01	62.00
C2	86.75	86.62	86.91	86.91
C3	80.17	80.67	80.43	80.38
C4	72.16	70.30	71.21	71.18
PCC	77.17	77.01	77.30	77.29

good semivariogram reconstruction ability of the deconvolution approach as well as the small errors in spectral unmixing in this experiment.

The SPM results of PSA, SPSAM, ICK, and NICK methods ($S = 8$) are provided in Fig. 16. Again, ICK utilized the fine spatial resolution semivariograms extracted from the reference map in Fig. 13(b). Similar to previous experiments, the PSA result appears to be locally smooth, and the SPSAM result contains cone-shaped patches. Generally, the ICK and NICK results are visually more in agreement with the reference distribution of land cover in Fig. 13(b). Table III lists the accuracy of the four SPM methods. Note that due to the inherent uncertainty in soft classification, in this experiment, all coarse pixels (including both mixed and nonmixed pixels) in Fig. 14 were included in the accuracy statistics. PSA produces the greatest accuracy (i.e., 72.16%) for class C4, whereas SPSAM produces the greatest accuracy (i.e., 80.67%) for class C3. However, the overall accuracy in terms of PCC of ICK and NICK is greater than PSA and SPSAM.

TABLE IV
COMPUTING TIME OF SPM METHODS IN EXPERIMENTS

	Size of coarse image	Zoom factor S	Number of classes	PSA	SPSAM	ICK	NICK		
							Deconvolution	ICK	Total
Experiment 1	75×75 pixels	8	4	300s	15s	40s	17s	40s	57s
Experiment 2	60×60 pixels	8	7	210s	6s	50s	14s	50s	54s
Experiment 3	50×50 pixels	8	4	130s	2s	27s	16s	27s	43s

V. DISCUSSION

A. Computing Efficiency

The computing efficiency is an important factor for SPM algorithm evaluation. Table IV lists the computing time of the four methods in each experiment. The computing burden of SPM algorithms is related to the image size and number of classes in the image. In the three experiments, SPSAM took the least time, as it is noniterative and is based on simple multiplication [22], [29], [38]. For PSA in each experiment, it took several minutes to converge to a satisfactory result. Both ICK and NICK are faster than PSA and need less than 1 min in each experiment. Compared with ICK, NICK requires more time as it involves the extra deconvolution process.

B. McNemar's Test

Here, McNemar's test [56] was used to show the statistical significance in accuracy for different SPM methods. The significance of difference between two classifiers (SPM is essentially a hard classification technique, but at the subpixel scale) is determined by

$$Z_{12} = \frac{f_{12} - f_{21}}{\sqrt{f_{12} + f_{21}}} \quad (15)$$

where f_{12} are the number of pixels that are correctly classified in result 1 but incorrectly classified in result 2, and f_{21} vice versa. Using the 95% confidence level, the difference between two SPM results is considered to be statistically significant if $|Z| > 1.96$.

The McNemar's test results for the five test images are shown in Table V. In each image, all pixels are included in the statistics for the calculation of the Z values. As can be observed from the values, ICK and NICK are generally able to produce more statistically significant SPM results than PSA and SPSAM. As for the comparison between the ICK and NICK results, their differences are considered to be statistically insignificant in the experiments.

C. Difference Between the Semivariograms Used in NICK and ICK

NICK does not need training images and uses the semivariogram obtained by deconvolution, based on the input proportion images for SPM. As mentioned in the introduction, the spatial structure information used in ICK-based SPM should be defined at the target spatial resolution and be representative of the studied area for SPM. In Section III-B, it was demonstrated that deconvolution provides a suitable means of converting

TABLE V
MCNEMAR'S TEST FOR SPM METHODS IN EXPERIMENTS

	Classifier 1	Classifier 2	f_{12}	f_{21}	Z_{12}
South Carolina	NICK	PSA	33309	28705	18.49
	NICK	SPSAM	25672	21799	17.78
	NICK	ICK	1249	1180	1.40
	ICK	PSA	33529	28994	18.14
	ICK	SPSAM	25785	21981	17.41
	SPSAM	PSA	34049	33318	2.82
Ohio	NICK	PSA	21487	19133	11.68
	NICK	SPSAM	16579	14386	12.46
	NICK	ICK	174	168	0.32
	ICK	PSA	21496	19148	11.65
	ICK	SPSAM	16634	14447	12.41
	SPSAM	PSA	21693	21532	0.77
Xuzhou suburb	NICK	PSA	15164	15653	-2.79
	NICK	SPSAM	12841	10561	14.90
	NICK	ICK	227	250	-1.05
	ICK	PSA	15139	15605	-2.66
	ICK	SPSAM	12825	10522	15.07
	SPSAM	PSA	15414	18183	-15.11
Xuzhou urban	NICK	PSA	16929	16569	1.97
	NICK	SPSAM	11918	11075	5.56
	NICK	ICK	611	655	-1.24
	ICK	PSA	16906	16502	2.21
	ICK	SPSAM	11923	11036	5.85
	SPSAM	PSA	17020	17503	-2.60
Liaoning	NICK	PSA	9342	9153	1.39
	NICK	SPSAM	7217	6777	3.72
	NICK	ICK	45	58	-1.28
	ICK	PSA	9344	9142	1.49
	ICK	SPSAM	7213	6760	3.83
	SPSAM	PSA	9651	9902	-1.80

the coarse spatial resolution semivariogram to the desired fine spatial resolution semivariogram. Thus, in the example given, the mismatch between the desired spatial resolution of the target semivariogram and the coarse spatial resolution of the available data was addressed by NICK. This necessitates a discussion of how the spatial structure characterized by the deconvolved fine spatial resolution semivariogram matches that of the reference fine spatial resolution semivariogram. This was investigated by analyzing the differences between the two types of semivariograms, measured by the RMSE. In the experiments, the deconvolved semivariogram was used in NICK, whereas the reference semivariogram was used in ICK.

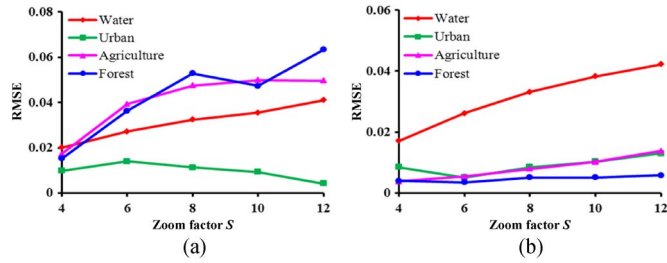


Fig. 17. RMSE between the fine spatial resolution semivariogram estimated by deconvolution and that extracted from fine spatial resolution training images. (a) South Carolina. (b) Ohio. (Red line) Water. (Green line) Urban. (Magenta line) Agriculture. (Blue line) Forest.

The South Carolina and Ohio maps were used for the analysis. The RMSE values for five zoom factors (i.e., $S = 4, 6, 8, 10,$ and 12) and four classes in the two areas are shown in Fig. 17. The RMSE between the two types of semivariograms increases in general as S increases, because the uncertainty in deconvolution increases correspondingly. Nevertheless, the RMSE values presented in the figure are not very large and are very small for small zoom factors. For the South Carolina map, most of the values are less than 0.05, and for the Ohio map, the values are less than 0.02 for the urban, agriculture, and forest classes. This indicates a relatively high degree of similarity between the two types of semivariograms. Hence, the spatial structure of classes characterized by the deconvolved fine spatial resolution semivariograms may be considered to be representative of the studied area, particularly for a small zoom factor in the experiment.

As can be found from the PCC of ICK and NICK, the two methods have similar accuracy. The accuracy of the two ICK-based SPM methods is related mainly to class probability estimation, which is determined by two parts: proportions and weights that are calculated based on the semivariogram [see (4)]. In ICK and NICK, the proportions are exactly the same, since they are performed on the same input coarse spatial resolution images. With respect to the two sets of weights in the ICK and NICK methods, they are derived from the semivariograms obtained by deconvolution and those extracted from the fine spatial resolution training images (reference land cover maps in the experiments), respectively. The two types of semivariograms used in ICK and NICK are close to each other, as can be found in Fig. 17 and as discussed above. The similar accuracy of the two methods in the experiments is thus attributed to the same proportions and similar semivariograms used.

D. Characteristics of NICK

In our previous research [37], it was mentioned that the ICK-based SPM method holds several advantages. Few parameters are involved in this model, and it is noniterative as the probabilities of class occurrence in subpixels are predicted by solving a system of equations via ICK [see (1) and (2)]. NICK has the same probability calculation process as ICK and, thus, the same benefits. The experimental results show that NICK consistently produces comparable SPM accuracy to ICK and higher accuracy than the well-known SPSAM method. The difference between the original ICK and the proposed NICK

method is the means of acquiring the required semivariogram. The acquisition of the semivariogram for NICK is realized by fully mining the available information in the coarse spatial resolution proportion images and does not require prior spatial structure information or training images. The deconvolution process in NICK is iterative and introduces several parameters, such as the number of iterations and threshold for the stopping condition. Therefore, the introduced iteration process and parameters are the cost of not using prior spatial structure information for NICK. Nevertheless, we can conclude that NICK inherits the advantage of ICK in terms of SPM accuracy and, more importantly, extends ICK to cases where the prior spatial structure information is unavailable. For these reasons, the newly developed geostatistics-based SPM method has great potential in real applications.

E. Future Research

The proposed NICK is shown to be a robust SPM method in this study, which produces consistently comparable SPM accuracy (in terms of PCC) to ICK in two separate experiments. This is good evidence of the effectiveness of the deconvolution-based NICK method. However, it is insufficient to reveal the generalizability of the proposed NICK method in all cases in the real world where land covers may be diversely distributed. It is essential to pay due attention to this problem.

In cases where the objects of interest are larger than the pixel size of the coarse spatial resolution input image (i.e., the well-known H-resolution case [9]), deconvolution is likely to lead to sufficiently reliable estimates of the fine resolution semivariogram. In cases where the objects of interest are smaller than the pixel size (i.e., the L-resolution case), deconvolution may lead to an underestimate of the semivariance in the fine resolution semivariogram. However, we note that both the ICK and NICK methods are defined for application in the H-resolution case only. Alternative pattern-matching-type algorithms are more suited to, and should be applied in, the L-resolution case. Moreover, it is not clear whether such differences will lead to significant underperformance of the NICK method itself, since we anticipate a high degree of robustness of the method to semivariogram estimation. Thus, in future research, further cases need to be tested, specifically to characterize the range of conditions under which the NICK method is likely to be suitable and to test the robustness of the NICK method to semivariogram estimation.

NICK also provides a promising new option for implementing ICK in downscaling of continua. As can be found from expression (3), it can predict continuous variables at a fine spatial resolution, given the input coarse spatial resolution image. Downscaling continua [39], such as downscaling surface temperature [57] or surface soil moisture [58], has gained increasing attention recently. Therefore, the proposed NICK method may be a promising approach for these applications.

VI. CONCLUSION

This paper has presented a NICK-based SPM method, in which the semivariogram used for ICK-derived probability

prediction is obtained by deconvolving the semivariogram extracted from the input coarse spatial resolution proportion images, rather than additional fine spatial resolution training images as in the original ICK method. Experimental results reveal that it is feasible to estimate the fine spatial resolution semivariogram by deconvolution for ICK-based SPM. The semivariogram observed at a coarse spatial resolution can be converted to the one required at the target fine spatial resolution such as to characterize the spatial structure of land cover, representative of the studied area. Tested with three groups of remote sensing images, the results of the new ICK method were found to have comparable SPM accuracy to the original ICK method. Thus, the proposed method enables the application of ICK in cases where no prior spatial structure information exists. Future research will focus on testing the NICK method in more cases and extending it to more problem sets (e.g., downscaling continua).

ACKNOWLEDGMENT

The authors would like to thank H. Jin from the College of Environmental Science and Forestry, State University of New York, Syracuse, NY, USA, for sharing the NLCD 2001 land cover maps, and M. Hao from the China University of Mining and Technology, Beijing, China, for providing the Liaoning Landsat data set. They would also like to thank Z. Miao from The Hong Kong Polytechnic University, Kowloon, Hong Kong, for proofreading the early version of this paper, as well as the handling editor and anonymous reviewers, whose valuable comments greatly improved this paper.

REFERENCES

- [1] P. Fisher, "The pixel: A snare and a delusion," *Int. J. Remote Sens.*, vol. 18, no. 3, pp. 679–685, Feb. 1997.
- [2] L. Wang, D. Liu, and Q. Wang, "Geometric method of fully constrained least squares linear spectral mixture analysis," *IEEE Trans. Geosci. Remote Sens.*, vol. 51, no. 6, pp. 3558–3566, Jun. 2013.
- [3] G. M. Foody, "Estimation of sub-pixel land cover composition in the presence of untrained classes," *Comput. Geosci.*, vol. 26, no. 4, pp. 469–478, May 2000.
- [4] J. Plaza, A. Plaza, R. Perez, and P. Martinez, "On the use of small training sets for neural network-based characterization of mixed pixels in remotely sensed hyperspectral images," *Pattern Recog.*, vol. 42, no. 11, pp. 3032–3045, Nov. 2009.
- [5] R. A. Schowengerdt, "On the estimation of spatial-spectral mixing with classifier likelihood functions," *Pattern Recog. Lett.*, vol. 17, no. 13, pp. 1379–1387, Nov. 1996.
- [6] M. Brown, H. Lewis, and S. Gunn, "Linear spectral mixture models and Support Vector Machine for remote sensing," *IEEE Trans. Geosci. Remote Sens.*, vol. 38, no. 5, pp. 2346–2360, Sep. 2000.
- [7] L. Wang, D. Liu, and Q. Wang, "Spectral unmixing model based on least squares support vector machine with unmixing residue constraints," *IEEE Geosci. Remote Sens. Lett.*, vol. 10, no. 6, pp. 1592–1596, Nov. 2013.
- [8] P. M. Atkinson, "Mapping sub-pixel boundaries from remotely sensed images," *Innov. GIS*, vol. 4, pp. 166–180, 1997.
- [9] P. M. Atkinson, "Issues of uncertainty in super-resolution mapping and their implications for the design of an inter-comparison study," *Int. J. Remote Sens.*, vol. 30, no. 20, pp. 5293–5308, 2009.
- [10] J. Verhoeve and R. De Wulf, "Land-cover mapping at sub-pixel scales using linear optimization techniques," *Remote Sens. Environ.*, vol. 79, no. 1, pp. 96–104, Jan. 2002.
- [11] A. J. Tatem, H. G. Lewis, P. M. Atkinson, and M. S. Nixon, "Multi-class land cover mapping at the sub-pixel scale using a Hopfield neural network," *Int. J. Appl. Earth Observ. Geoinf.*, vol. 3, no. 2, pp. 184–190, 2001.
- [12] A. M. Muad and G. M. Foody, "Impact of land cover patch size on the accuracy of patch area representation in HNN-based super resolution mapping," *IEEE J. Sel. Topics Appl. Earth Observ. Remote Sens.*, vol. 5, no. 5, pp. 1418–1427, Oct. 2012.
- [13] M. Q. Nguyen, P. M. Atkinson, and H. G. Lewis, "Superresolution mapping using a Hopfield neural network with LIDAR data," *IEEE Geosci. Remote Sens. Lett.*, vol. 2, no. 3, pp. 366–370, Jul. 2005.
- [14] F. Ling, Y. Du, F. Xiao, H. Xue, and S. Wu, "Super-resolution land-cover mapping using multiple sub-pixel shifted remotely sensed images," *Int. J. Remote Sens.*, vol. 31, no. 19, pp. 5023–5040, Jun. 2010.
- [15] K. C. Mertens, L. P. C. Verbeke, E. I. Ducheyne, and R. De Wulf, "Using genetic algorithms in sub-pixel mapping," *Int. J. Remote Sens.*, vol. 24, no. 21, pp. 4241–4247, 2003.
- [16] P. M. Atkinson, "Sub-pixel target mapping from soft-classified, remotely sensed imagery," *Photogramm. Eng. Remote Sens.*, vol. 71, no. 7, pp. 839–846, 2005.
- [17] Y. Makido, A. Shortridge, and J. P. Messina, "Assessing alternatives for modeling the spatial distribution of multiple land-cover classes at sub-pixel scales," *Photogramm. Eng. Remote Sens.*, vol. 73, no. 8, pp. 935–943, 2007.
- [18] Z. Shen, J. Qi, and K. Wang, "Modification of pixel-swapping algorithm with initialization from a sub-pixel/pixel spatial attraction model," *Photogramm. Eng. Remote Sens.*, vol. 75, no. 5, pp. 557–567, 2009.
- [19] A. Villa, J. Chanussot, J. A. Benediktsson, C. Jutten, and R. Dambreville, "Unsupervised methods for the classification of hyperspectral images with low spatial resolution," *Pattern Recog.*, vol. 46, no. 6, pp. 1556–1568, Jun. 2013.
- [20] F. Ling, F. Xiao, Y. Du, H. Xue, and X. Ren, "Waterline mapping at the subpixel scale from remote sensing imagery with high-resolution digital elevation models," *Int. J. Remote Sens.*, vol. 29, no. 6, pp. 1809–1815, Mar. 2008.
- [21] Y. Xu and B. Huang, "A spatio-temporal pixel-swapping algorithm for subpixel land cover mapping," *IEEE Geosci. Remote Sens. Lett.*, vol. 11, no. 2, pp. 474–478, Feb. 2014.
- [22] K. C. Mertens, B. D. Baset, L. P. C. Verbeke, and R. De Wulf, "A sub-pixel mapping algorithm based on sub-pixel/pixel spatial attraction models," *Int. J. Remote Sens.*, vol. 27, no. 15, pp. 3293–3310, Aug. 2006.
- [23] Z. Mahmood, M. A. Akhter, G. Thoonen, and P. Scheunders, "Contextual subpixel mapping of hyperspectral images making use of a high resolution color image," *IEEE J. Sel. Topics Appl. Earth Observ. Remote Sens.*, vol. 6, no. 2, pp. 779–791, Apr. 2013.
- [24] T. Kasetkasem, M. K. Arora, and P. K. Varshney, "Super-resolution land-cover mapping using a Markov random field based approach," *Remote Sens. Environ.*, vol. 96, no. 3/4, pp. 302–314, Jun. 2005.
- [25] V. A. Tolpekin and A. Stein, "Quantification of the effects of land-cover-class spectral separability on the accuracy of Markov-random-field based superresolution mapping," *IEEE Trans. Geosci. Remote Sens.*, vol. 47, no. 9, pp. 3283–3297, Sep. 2009.
- [26] J. P. Ardila, V. A. Tolpekin, W. Bijker, and A. Stein, "Markov-random-field-based super-resolution mapping for identification of urban trees in VHR images," *ISPRS J. Photogramm. Remote Sens.*, vol. 66, no. 6, pp. 762–775, Nov. 2011.
- [27] L. Wang and Q. Wang, "Subpixel mapping using Markov random field with multiple spectral constraints from subpixel shifted remote sensing images," *IEEE Geosci. Remote Sens. Lett.*, vol. 10, no. 3, pp. 598–602, May 2013.
- [28] X. Li, Y. Du, and F. Ling, "Super-resolution mapping of forests with bitemporal different spatial resolution images based on the spatial-temporal Markov random field," *IEEE J. Sel. Topics Appl. Earth Observ. Remote Sens.*, vol. 7, no. 1, pp. 29–39, Jan. 2014.
- [29] Q. Wang, L. Wang, and D. Liu, "Particle swarm optimization-based sub-pixel mapping for remote-sensing imagery," *Int. J. Remote Sens.*, vol. 33, no. 20, pp. 6480–6496, Oct. 2012.
- [30] G. M. Foody, A. M. Muslim, and P. M. Atkinson, "Super-resolution mapping of the waterline from remotely sensed data," *Int. J. Remote Sens.*, vol. 26, no. 24, pp. 5381–5392, Dec. 2005.
- [31] Y. F. Su, G. M. Foody, A. M. Muad, and K. S. Cheng, "Combining pixel swapping and contouring methods to enhance super-resolution mapping," *IEEE J. Sel. Topics Appl. Earth Observ. Remote Sens.*, vol. 5, no. 5, pp. 1428–1437, Oct. 2012.
- [32] Y. Shao and R. S. Lunetta, "Sub-pixel mapping of tree canopy, impervious surfaces, and cropland in the Laurentian Great Lakes basin using MODIS time-series data," *IEEE J. Sel. Topics Appl. Earth Observ. Remote Sens.*, vol. 4, no. 2, pp. 336–347, Jun. 2011.
- [33] D. Nigussie, R. Zurita-Milla, and J. G. P. W. Clevers, "Possibilities and limitations of artificial neural networks for subpixel mapping of land cover," *Int. J. Remote Sens.*, vol. 32, no. 22, pp. 7203–7226, Nov. 2011.

- [34] P. M. Atkinson, "Super-resolution land cover classification using the two-point histogram," *GeoENV IV: Geostat. Environ. Appl.*, vol. 13, pp. 15–28, 2004.
- [35] A. Boucher and P. C. Kyriakidis, "Super-resolution land cover mapping with indicator geostatistics," *Remote Sens. Environ.*, vol. 104, no. 3, pp. 264–282, Oct. 2006.
- [36] H. Jin, G. Mountrakis, and P. Li, "A super-resolution mapping method using local indicator variograms," *Int. J. Remote Sens.*, vol. 33, no. 24, pp. 7747–7773, Dec. 2012.
- [37] Q. Wang, W. Shi, and L. Wang, "Indicator cokriging-based subpixel land cover mapping with shifted images," *IEEE J. Sel. Topics Appl. Earth Observ. Remote Sens.*, vol. 7, no. 1, pp. 327–339, Jan. 2014.
- [38] Q. Wang, W. Shi, and L. Wang, "Allocating classes for soft-then-hard subpixel mapping algorithms in units of class," *IEEE Trans. Geosci. Remote Sens.*, vol. 52, no. 5, pp. 2940–2959, May 2014.
- [39] P. M. Atkinson, "Downscaling in remote sensing," *Int. J. Appl. Earth Observ. Geoinf.*, vol. 22, pp. 106–114, Jun. 2013.
- [40] Y. Ge, "Sub-pixel land-cover mapping with improved proportion images upon multiple-point simulation," *Int. J. Appl. Earth Observ. Geoinf.*, vol. 22, pp. 115–126, 2013.
- [41] A. Boucher and P. C. Kyriakidis, "Integrating fine scale information in super-resolution land-cover mapping," *Photogramm. Eng. Remote Sens.*, vol. 73, no. 8, pp. 913–921, 2008.
- [42] Y. Ge and H. Bai, "Multiple-point simulation-based method for extraction of objects with spatial structure from remotely sensed imagery," *Int. J. Remote Sens.*, vol. 32, no. 8, pp. 2311–2335, Apr. 2011.
- [43] A. G. Journel and C. J. Huijbregts, *Mining Geostatistics*. London, U.K.: Academic Press, 1978.
- [44] P. Goovaerts, "Kriging and semivariogram deconvolution in presence of irregular geographical units," *Math. Geosci.*, vol. 40, no. 1, pp. 101–128, 2008.
- [45] J. B. Collins and C. E. Woodcock, "Geostatistical estimation of resolution-dependent variance in remotely sensed images," *Photogramm. Eng. Remote Sens.*, vol. 65, no. 1, pp. 41–50, Jan. 1999.
- [46] P. N. Truong, G. B. M. Heuvelink, and E. Pebesma, "Bayesian area-to-point kriging using expert knowledge as informative priors," *Int. J. Appl. Earth Observ. Geoinf.*, vol. 30, pp. 128–138, Aug. 2014.
- [47] P. C. Kyriakidis, "A geostatistical framework for area-to-point spatial interpolation," *Geograph. Anal.*, vol. 36, no. 3, pp. 259–289, Jul. 2004.
- [48] X. Xu, Y. Zhong, L. Zhang, and H. Zhang, "Sub-pixel mapping based on a MAP model with multiple shifted hyperspectral imagery," *IEEE J. Sel. Topics Appl. Earth Observ. Remote Sens.*, vol. 6, no. 2, pp. 580–593, Apr. 2013.
- [49] Q. Wang, W. Shi, and P. M. Atkinson, "Sub-pixel mapping of remote sensing images based on radial basis function interpolation," *ISPRS J. Photogramm. Remote Sens.*, vol. 92, pp. 1–15, Jun. 2014.
- [50] C. Homer, C. Huang, L. Yang, B. Wylie, and M. Coan, "Development of a 2001 National Land Cover Database for the United States," *Photogramm. Eng. Remote Sens.*, vol. 70, no. 7, pp. 829–840, Jul. 2004.
- [51] Q. Wang and W. Shi, "Utilizing multiple subpixel shifted images in subpixel mapping with image interpolation," *IEEE Geosci. Remote Sens. Lett.*, vol. 11, no. 4, pp. 798–802, Apr. 2014.
- [52] Y. Zhong and L. Zhang, "Remote sensing image subpixel mapping based on adaptive differential evolution," *IEEE Trans. Syst. Man Cybern. B, Cybern.*, vol. 42, no. 5, pp. 1306–1329, Oct. 2012.
- [53] Q. Wang, W. Shi, and H. Zhang, "Class allocation for soft-then-hard subpixel mapping algorithms with adaptive visiting order of classes," *IEEE Geosci. Remote Sens. Lett.*, vol. 11, no. 9, pp. 1494–1498, Sep. 2014.
- [54] H. Zhang, W. Shi, Y. Wang, M. Hao, and Z. Miao, "Classification of very high spatial resolution imagery based on a new pixel shape feature set," *IEEE Geosci. Remote Sens. Lett.*, vol. 11, no. 5, pp. 940–944, May 2014.
- [55] D. C. Heinz and C.-I. Chang, "Fully constrained least squares linear spectral mixture analysis method for material quantification in hyperspectral imagery," *IEEE Trans. Geosci. Remote Sens.*, vol. 39, no. 3, pp. 529–545, May 2001.
- [56] G. M. Foody, "Thematic map comparison evaluating the statistical significance of differences in classification accuracy," *Photogramm. Eng. Remote Sens.*, vol. 70, no. 5, pp. 627–633, 2004.
- [57] A. Kallel, C. Ottlé, S. Le Hégarat-Masclé, F. Maignan, and D. Courault, "Surface temperature downscaling from multiresolution instruments based on Markov models," *IEEE Trans. Geosci. Remote Sens.*, vol. 51, no. 3, pp. 1588–1612, Mar. 2013.
- [58] C. Song, L. Jia, and M. Menenti, "Retrieving high-resolution surface soil moisture by downscaling AMSR-E brightness temperature using MODIS LST and NDVI data," *IEEE J. Sel. Topics Appl. Earth Observ. Remote Sens.*, vol. 7, no. 3, pp. 935–942, Mar. 2014.



Qunming Wang received the B.S. and M.S. degrees from Harbin Engineering University, Harbin, China, in 2010 and 2012, respectively. He is currently working toward the Ph.D. degree in the Department of Land Surveying and Geo-Informatics, The Hong Kong Polytechnic University, Kowloon, Hong Kong.

His current research interests focus on remote sensing image analysis, pattern recognition, and geostatistics. From June 2013 to December 2013, he was a visiting Ph.D. student in geography and environment with the University of Southampton, Southampton, U.K.

Mr. Wang was the recipient of the Excellent Master Dissertation Award and the Excellent Graduates in Heilongjiang Province, China, in 2012. He has been awarded the hyper-competitive Hong Kong Ph.D. Fellowship. He serves as a reviewer for the IEEE TRANSACTIONS ON GEOSCIENCE AND REMOTE SENSING, the IEEE TRANSACTIONS ON CYBERNETICS, the IEEE GEOSCIENCE AND REMOTE SENSING LETTERS, the IEEE JOURNAL OF SELECTED TOPICS IN APPLIED EARTH OBSERVATION AND REMOTE SENSING, *Photogrammetric Engineering and Remote Sensing*, the *International Journal of Remote Sensing*, and *Remote Sensing Letters*.



Peter M. Atkinson received the B.Sc. degree in geography from the University of Nottingham, Nottingham, U.K., in 1986; the Ph.D. degree from the University of Sheffield (NERC CASE award with Rothamsted Experimental Station), Sheffield, U.K., in 1990; and the MBA degree from the University of Southampton, Southampton, U.K., in 2012.

He is currently a Professor of geography with the University Southampton and a Visiting Fellow with Green Templeton College, Oxford University, Oxford, U.K. He has published over 160 peer-

reviewed articles in international scientific journals and around 50 refereed book chapters. He has also edited nine journal special issues and eight books. The main focus of his research is in remote sensing, geographical information science, and spatial (and space–time) statistics applied to a range of environmental science and socioeconomic problems.

Dr. Atkinson has organized several major international conferences in Southampton, including GeoComputation in 2003 and GeoENV in 2008. He is an Associate Editor for *Computers and Geosciences* and sits on the editorial board of several other journals, including *Geographical Analysis*, *Spatial Statistics*, the *International Journal of Applied Earth Observation and Geoinformation*, and *Environmental Informatics*. He also sits on various international scientific committees.



Wenzhong Shi received the Ph.D. degree from the University of Osnabrück, Vechta, Germany, in 1994.

He is a Chair Professor in geographic information systems (GIS) and remote sensing with the Department of Land Surveying and Geo-Informatics, The Hong Kong Polytechnic University, Kowloon, Hong Kong. He has published over 100 SCI papers and ten books. His current research interests include GIS and remote sensing, uncertainty and spatial data quality control, and image processing for high-resolution satellite images.

Dr. Shi received the State Natural Science Award from the State Council of China in 2007 and The Wang Zhizhuo Award from the International Society for Photogrammetry and Remote Sensing in 2012.